LITHIUM-ION BATTERY PERFORMANCE:
DEPENDENCE ON MATERIAL SYNTHESIS AND POST-TREATMENT METHODS



Dr. Qifeng Zhang, Mr. Evan Uchaker, and Dr. Guozhong Cao*
Department of Materials Science and Engineering
University of Washington
Seattle, WA 98195-2120
*Email: gzcao@u.washington.edu

Introduction

Lithium-ion batteries represent a group of electrochemical devices used for electricity storage and have attracted a lot of attention in the past two decades due to their portability, rechargeability, and low cost. The major effort on lithium-ion batteries (LIBs) at present is to optimize the materials that form the cathode or anode films to increase the battery capacity to reach the theoretical maximum with enhanced cyclic stability in relation to lithium-ion intercalation and deintercalation. It has been proven that both the capacity and stability of LIBs are closely related to the materials being used to form the electrodes. More specifically, the battery capacity and stability greatly rely on chemical composition, microstructure, crystallinity, and defects of the electrode materials. This review features several materials involved in our work on LIBs. The performance of LIBs can be improved to a large extent by: (1) tailoring the microstructure; (2) controlling the crystallinity of electrode materials; and/or (3) introducing suitable defects to the materials, thereby enhancing the electron and mass transport to improve the battery stability.

MnO_2 Nanowall Arrays

One of the most outstanding advantages of nanostructured materials is that they can form porous films that result in extremely high internal surface area. This is particularly important for electrochemical devices such as LIBs which involve a faradaic reaction at the solid/liquid interface formed by electrode film and liquid electrolyte. MnO_2 is one of several commonly used LIB materials. However, MnO_2 (Aldrich Prod. No. 529664) microsized particles prepared using conventional slurry methods to form electrode film demonstrate relatively low discharge capacities of ~120 mAh/g.[1] MnO_2 nanowall arrays are a novel nanostructure and reportedly achieve both a significantly higher discharge capacity and good cyclic stability due to their large surface area and short pathways for lithium-ion diffusion. The approximately amorphous phase structure of the nanowalls results from the cathodic electrodeposition method used to fabricate the electrode film.[2]

The MnO_2 nanowall arrays were prepared using an electrodeposition method from a solution containing 0.1 M manganese acetate (Aldrich Prod. No. 330825) and sodium sulfate (Sigma-Aldrich Prod. No. 793531) under a constant voltage ranging from –1.2 to 2.2 V for 15 min. The MnO_2 nanowall arrays were grown on a platinum foil substrate at the cathodic side; a separate platinum foil was used in anode of the deposition system. The deposited film was washed with deionized water and then air-dried without any further treatment. **Figure 1** shows a typical SEM image of the as-prepared MnO_2 nanowall array film. It reveals the porous structure of the electrode film is comprised of vertically grown MnO_2 walls of 50–100 nm thickness. The film was also characterized using X-ray diffraction and found to be approximately amorphous, although the peaks presented a slight match with those of ε-MnO_2.[2] The thermogravimetric analysis revealed the as-produced nanowall arrays had a chemical composition of $MnO_2{\cdot}nH_2O$ with n≈0.5.

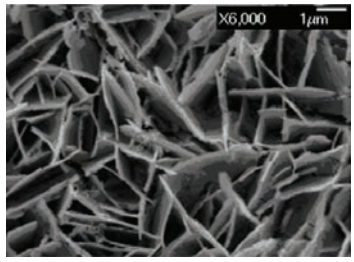

Figure 1. Morphology and structure of MnO_2 nanowall arrays produced from cathodic electrodepostion.[2]

Formation of the nanowall structure is a result of water electrolysis-induced precipitation of MnO_2 at the cathode side, where H_2 gas bubbles generated due to water electrolysis play an important role in the formation of the porous nanowall structure.[2,3] The height of the nanowalls is dependent on both the applied bias and the deposition time. For example, the use of –1.2 V for 15 min. led to ~500 nm high nanowalls, which increased to 2.5 μm with the applied bias of –1.8 V for 15 min. However, the increase in nanowall height didn't result in an increase in the internal surface area of the electrode film due to an increase in the nanowall thickness. The nanowall thickness is also a function of the concentration of the solution. High concentration generally results in thick nanowalls and leads to low internal surface area.[3]

Electrochemical characterization of the MnO_2 nanowall array revealed excellent charge/discharge properties in less crystallized nanowall structures. The nanowall array of ~2.5 μm height (i.e., film thickness) deposited at –1.8 V presented an initial discharge capacity of 270 mAh/g at a rate of 0.1 mA/cm^2 (corresponding to a current density of 76 mA/g). The capacity remained as high as 220 mAh/g even over 50 cycles, which significantly exceeds the typical capacity of 120 mAh/g for a traditional MnO_2 electrode. These results indicate MnO_2 nanowall arrays are a

TO ORDER: Contact your local Sigma-Aldrich office or visit aldrich.com/matsci.

promising material for lithium-ion intercalation/deintercalation due to both their high capacity and good stability,[2] which are attributed to: (1) the large surface area of the porous nanowall structure; (2) short pathways for lithium-ion diffusion; and (3) the approximately amorphous structure of the nanowalls, making the electrode film less well packed and, therefore, possess a greater capacity for structural accommodation during lithium-ion intercalation/deintercalation.

TiO_2 Nanotube Arrays

Annealing Temperature Effect

TiO_2 nanotube arrays have generated significant interest for use in electrochemical and photoelectrochemical devices due to their ordered one-dimensional structure that possesses a large internal surface area and may provide direct pathways for ion and electron transport.[4,5] The significant attention received by TiO_2 nanotube arrays is also attributed to their ease of fabrication through a simple anodization method. The nanotube diameter, length, and wall thickness can be readily controlled by adjusting the recipe of electrolyte, applied voltage, and time for anodization. For LIB application, it has been found that in addition to the structural parameters such as nanotube diameter, length, and distribution density, both the capacity and the cyclic stability of an electrode film consisting of TiO_2 nanotube arrays are also affected by the post-treatment parameters.[6,7]

Figure 2A shows a typical SEM image of TiO_2 nanotube array produced using anodization with an electrolyte containing 0.1 M KF and 1.0 M $NaHSO_4$, at a constant potential of 20 V, for 1 hr. The nanotubes are ~100 nm in diameter and 1.1 µm in length. The direct use of the as-deposited TiO_2 nanotube array in a lithium-ion battery results in an initial discharge capacity of ~202 mAh/g, which degrades very quickly to 40 mAh/g after 50 cycles.[7] The poor cyclic stability is attributed to the amorphous phase of the as-deposited TiO_2 nanotube array, which results in an irreversible lithium-ion intercalation and deintercalation corresponding with literature results on amorphous TiO_2.[8] Heat treatment of TiO_2 nanotube arrays is an effective method for increasing both the capacity and the cyclic stability of the electrode film. **Figure 2B** shows the result of samples annealed in N_2 at 300 °C, 400 °C, and 500 °C. All the annealed samples present much better cyclic stability compared to the as-prepared sample. Although the initial capacities for the samples annealed at 400 °C and 500 °C are relatively low compared to the unannealed material, the capacities of the annealed samples are significantly higher after 50 cycles. The optimal temperature for heat treatment, 300 °C, leads to a high initial capacity (~240 mAh/g); a good capacity of 148 mAh/g is retained even after 50 cycles. The decrease in capacity of samples annealed at 400 °C and 500 °C compared to the sample annealed at 300 °C, is attributed to the reduced internal surface area.[6] Therefore, to achieve the best LIB performance with anodization-produced TiO_2 nanotube arrays, annealing at a high temperature is necessary to improve the cyclic stability. However, there is an optimal temperature which, on one hand, ensures the nanotube arrays gain the desired crystallinity and, on the other hand, makes sure the nanotube arrays possess large internal surface area for highly efficient faradaic reaction.

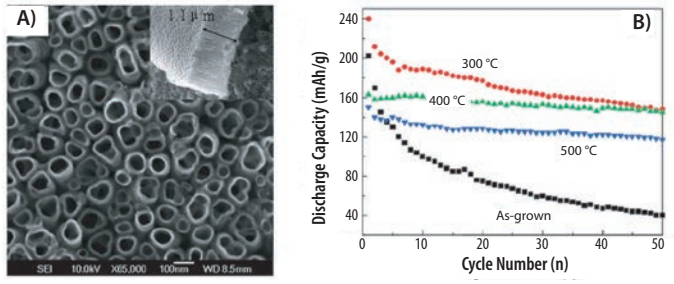

Figure 2. A) SEM image of a TiO_2 nanotube array and **B)** the dependence of discharge capacity and cyclic stability on annealing temperature of the TiO_2 nanotube array.[6]

Annealing Atmosphere Effect

In addition to the annealing temperature, the LIB performance of TiO_2 nanotube arrays is also sensitive to the annealing atmosphere. Compared to annealing in N_2 mentioned above, annealing the anodization-produced TiO_2 nanotube array in CO results in improved battery capacity.

The comparison was carried out between two TiO_2 nanotube array samples annealed in N_2 and CO, respectively, at 400 °C for 3 hr. **Figure 3** shows the charge/discharge properties and the cyclic stability of the samples annealed in N_2 and in CO. It can be seen that the initial capacity of electrode film consisting of a TiO_2 nanotube array annealed in CO is higher than the sample annealed in N_2 (~223 mAh/g in CO vs. 164 mAh/g in N_2). The cyclic stability of the sample annealed in CO is similar to that of the sample annealed in N_2 and, as a result, the discharge capacity of the sample annealed in CO after 50 cycles is significantly higher than the sample annealed in N_2. XPS analysis reveals that, due to the reduction capability of CO, the annealing in CO results in the Ti^{3+} state surface defect and Ti-carbon species in the TiO_2. The presence of the Ti^{3+} surface defect and Ti-carbon species appears to enhance the electron transport of the TiO_2 nanotubes and, thus, facilitates the electrochemical reaction with respect to the lithium-ion intercalation/deintercalation process. The impedance spectra show the sample annealed in CO possesses significantly lower resistance than that annealed in N_2,[7] which is consistent with the XPS analysis.

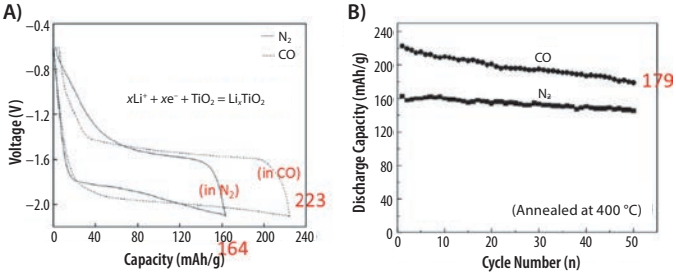

Figure 3. Enhanced LIB performance of TiO_2 nanotube arrays annealed in CO. **A)** The first cycle charge/discharge properties and **B)** cyclic stability of TiO_2 nanotube arrays annealed in N_2 and CO.[7]

V_2O_5 Xerogel Films

V_2O_5 is a rather important material that has been extensively studied for LIB application due to its layered structure. V_2O_5 xerogel films easily can be produced from a V_2O_5 solution by dissolving V_2O_5 powder (Aldrich Prod. No. 204854) in an aqueous solution containing H_2O_2 and drop-casting the solution onto a substrate to form a wet film.[9] The heat treatment of the wet film results in the formation of the V_2O_5 xerogel film. It has been also found that different atmospheres employed to heat-treat the V_2O_5 wet films may significantly influence the LIB performance. **Figure 4** shows the difference in the V_2O_5 films annealed in air and in N_2. It should be emphasized that both V_2O_5 films were prepared with the same precursor solution and procedure of drop-casting the V_2O_5 solution onto FTO glass substrates.[10] Optical absorption spectra characterization revealed that, compared with the sample annealed in air, the film annealed in N_2 presented a longer cut-off in wavelength, meaning a relatively narrower band gap of the latter (2.28 eV for annealed in N_2 vs. 2.37 eV for annealed in air), as seen in **Figure 4A**. The yellow color of the air-annealed sample and the dark green color of the N_2-annealed sample infers that the air-annealed V_2O_5 film primarily contains V^{5+}, while the N_2-annealed sample contains some vanadium in lower valences, such as V^{4+} and V^{3+}.

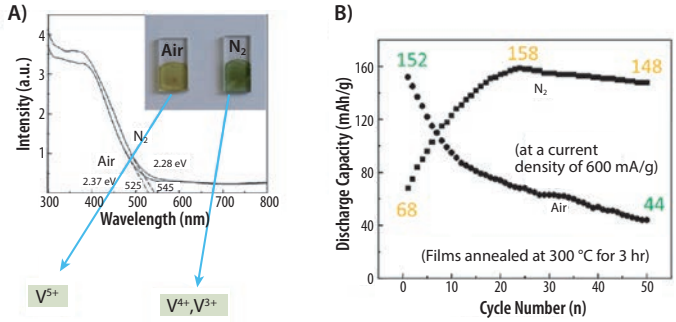

Figure 4. A comparison of the lithium-ion battery performance between V_2O_5 films annealed in air and in N_2: **A)** optical absorption spectra and **B)** lithium-ion cyclic properties of V_2O_5 films annealed in air and N_2.[10]

Figure 4B shows a comparison of the cyclic properties of the samples annealed in air and in N_2 over the first 50 cycles. The sample annealed in air presents an initial discharge capacity of ~152 mAh/g but degraded very quickly to only 44 mAh/g at 50 cycles. In contrast, the sample annealed in N_2 shows a low initial capacity of ~68 mAh/g; however, the capacity increased significantly during the first 24 cycles and reached 158 mAh/g. The capacity remained at a high level afterward, dropping a mere 10 mAh/g after 50 cycles, which indicates good cyclic stability of the N_2-annealed sample.

It is believed that annealing the V_2O_5 film in N_2 results in better performance than the film annealed in air due to the presence of low valence V ions, which induce impurity energy levels in the band gap of V_2O_5 and lead to the enhancement in capability for electron transport. This is the same as the case of TiO_2 nanotubes annealed in CO mentioned previously. The films annealed in different atmospheres were also analyzed with electrochemical impedance spectra, which revealed the electrode resistance of the film annealed in N_2 is about 30% lower than that of the film annealed in air.[10]

Besides annealing in N_2, Mn doping has also been proven effective in creating low valence V ions in the V_2O_5 film, thereby enhancing LIB performance.[11] The introduction of Mn in V_2O_5 is achieved by adding a soluble Mn salt (e.g., manganese acetate) into the aforementioned V_2O_5 solution during film preparation. **Figure 5** shows the discharge capacities of both a pure V_2O_5 film and an Mn-doped V_2O_5 film over the first 50 cycles. Both films were annealed at 250 °C for 3 hr in air. The initial capacities, 138 mAh/g for the doped film and 145 mAh/g for the undoped film, are very close. However, the Mn-doped film presented much better cyclic stability compared to the undoped film. After 50 cycles the capacity of Mn-doped film remained 135 mAh/g; whereas it dropped to 86 mAh/g for the undoped film. The improved cyclic stability is due to Mn doping of the V_2O_5. XPS analysis revealed there are coexistent V^{5+} and V^{4+} in the Mn-doped V_2O_5, although it is not clear how the Mn dopant results in low valence V.

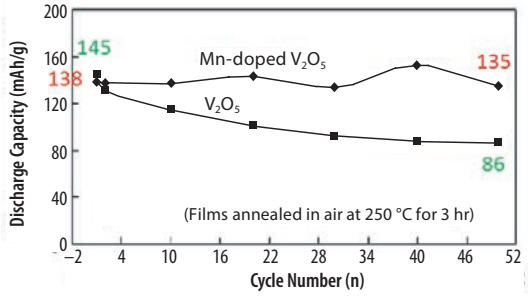

Figure 5. Enhanced cyclic stability of Mn-doped V_2O_5 film.[11]

Nanostructured V_2O_5

V_2O_5 Nanofibers

Electrospinning is a widely applied technique for the fabrication of one-dimensional (1D) nanostructures. An outstanding feature of 1D nanostructures developed for LIB is the resulting electrode films represent a good compromise between internal surface area and porosity. Electrode films comprised of 1D nanostructures possess both a large internal surface area (although it is usually smaller compared to that of nanoparticle films), suitable porous structure, and higher porosity than that of nanoparticle films. The high porosity is important as it allows the electrolyte to diffuse efficiently. Nanostructured V_2O_5 in the form of nanofibers is one example that demonstrates an electrode film with 1D nanostructures can outperform dense films or films comprised of nanoparticles.

V_2O_5 nanofibers can be prepared using electrospinning techniques by employing a V_2O_5 solution. In order to form the fiber structure, a polymer additive is often used to increase the viscosity of the V_2O_5 solution. Poly(vinylpyrrodidone) (PVP) (**Aldrich Prod. Nos.** 234257, 856568, and 437190) is a readily available polymer proven to work for this purpose.[12] The polymer additive is removed from the product by sintering the nanofiber powder at high temperatures (~500 °C) in air. **Figure 6A** shows SEM images of V_2O_5 nanofibers prepared with an electrospinning method. The image indicates the nanofibers are: (1) several tens of micrometers in length and ~350 nm in diameter after sintering; (2) comprised of interconnected V_2O_5 nanocrystals; and (3) the resultant film is well structured to provide large internal surface area and porosity. BET characterization revealed the surface area of the as-prepared V_2O_5 nanofibers to be 97 m^2/g.

TO ORDER: Contact your local Sigma-Aldrich office or visit aldrich.com/matsci.

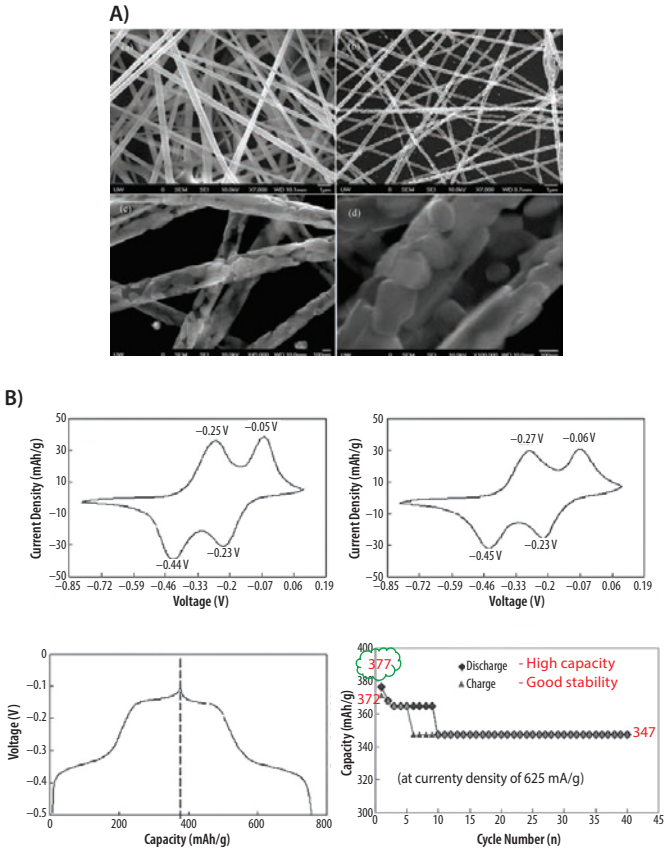

Figure 6. V_2O_5 nanofibers prepared with an electrospinning method for lithium-ion battery. **A)** SEM images of V_2O_5 nanofibers before and after being annealed (at 500 °C for 1 hr in air). **B)** Cyclic voltammetry curves and charge/discharge properties of the V_2O_5 nanofibers at a current density of 625 mA/g.[12]

LIB performance of the V_2O_5 nanofibers is shown in **Figure 6B**. Two anodic oxidation peaks located at –0.25 V and –0.05 V (vs. Ag/AgCl) corresponding to Li^+ deintercalation, and two cathodic reduction peaks located at –0.44 V and –0.23 V corresponding to Li^+ intercalation clearly can be seen on the cyclic voltammogram curves.[12] All these redox peaks are well defined. The voltages of redox peaks show only a negligible shift even after 40 cycles. The current densities also change only slightly. From the cyclic test, it can be seen that after the 9th cycle the discharge capacity remains at a high capacity (~347 mAh/g), which implies excellent cyclic stability and reversibility of the V_2O_5 nanofiber electrode film. The superior performance of the V_2O_5 nanofiber electrode, which is significantly better than that of the aforementioned V_2O_5 xerogel films and other V_2O_5 nanostructures (such as V_2O_5 nanotube arrays, nanocable arrays, and nanorod arrays[13,14]), is believed to arise from the high internal surface area provided by the nanofibers and ideal porosity of the electrode film comprised of these nanofibers. The high porosity enables the lithium ion intercalation and deintercalation to take place efficiently.

Nanoporous V_2O_5 Films

The advantage of nanostructured materials for LIB are further demonstrated by employing V_2O_5 films prepared with the same V_2O_5 solution used for drop-casting described previously[10,11] using a cathodic deposition method.[15] The films were deposited onto FTO glass substrates under a voltage of –2.4 V. Such a voltage results in water electrolysis and generates H_2 gas bubbles at the cathode, which is believed to cause the formation of nanosized pores in the films. The films were annealed at 500 °C to achieve desired crystallinity.

Figure 7A shows a typical SEM image of the as-prepared nanoporous V_2O_5 film. It reveals the film is comprised of nanosized crystallites of 20–30 nm diameter and contains pores on the order of 10 nm. While no other special structural feature is found on the film, interestingly, it delivered an extremely high initial capacity of ~402 mAh/g, and even after 200 cycles the capacity remained as high as 240 mAh/g (**Figure 7B**).[15] Such capacities are more than twice as high as that of V_2O_5 xerogel films[10] and, to some extent, are also higher than that of V_2O_5 nanofibers produced using electrospinning.[12] The cathodic deposition method is very simple, low cost, reliable, and compatible with mass production. The film also demonstrated good capacity at high current densities. For example, it showed a capacity of ~120 mAh/g at 10.5 A/g (70 C) (**Figure 7C**). The high internal surface area of the V_2O_5 nanoporous films is believed to be the main reason for the superb LIB performance. However, in addition to high surface area, the presence of tetravalent vanadium ions (V^{4+}) in the as-deposited film (before annealing) may also contribute to the high performance of V_2O_5 nanoporous films by catalyzing the growth of the V_2O_5 film during the electrochemical deposition process and enabling the formation of hierarchically structured electrode film with stacking flakes consisting of V_2O_5 nanoparticles.[15]

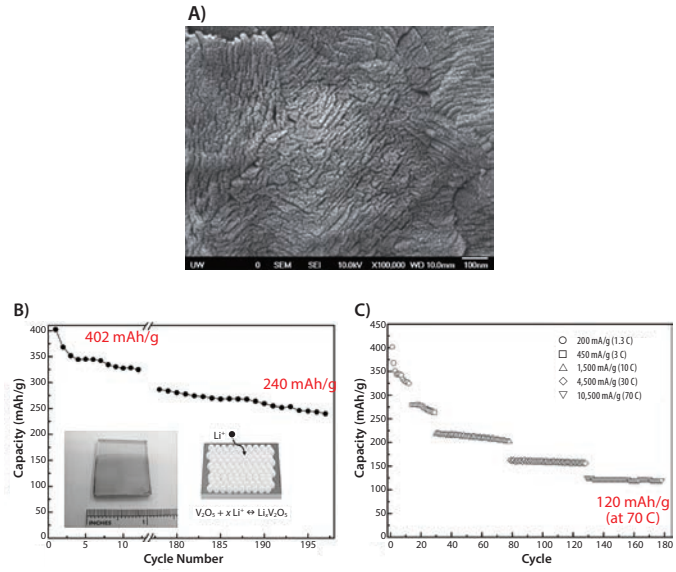

Figure 7. Nanoporous V_2O_5 film for lithium-ion battery application: **A)** SEM image of nanoporous V_2O_5 film; **B)** cyclic capacities at a current density of 200 mA/g (1.3 C); and **C)** cyclic capacities at different current densities up to 10.5 A/g (70 C).[15]

$LiFePO_4$/C Nanocomposites

$LiFePO_4$/C nanocomposites are another example demonstrating the optimization of post-treatment parameters is critically important to achieving high performance in LIBs. The fabrication of $LiFePO_4$/C nanocomposites was carried out by: (1) adding L-ascorbic acid ($C_6H_8O_6$) to a solution containing lithium hydroxide monohydrate ($LiOH{\cdot}H_2O$, Aldrich Prod. No. 254274), ferric nitrate $Fe(NO_3)_3{\cdot}9H_2O$ (Aldrich Prod. No. 529303), and phosphoric acid (H_3PO_4; (2) refluxing the mixture at 60 °C for 1 hr to attain a solution of $LiFePO_4$ (Aldrich Prod. No. 759546) with carbon; and (3) drop-casting and annealing the films in N_2.[16] L-ascorbic acid plays a role in this synthesis by reducing the iron ions from Fe^{3+} to Fe^{2+} and also serving as a source of carbon.

Figure 8 shows the SEM characterization of $LiFePO_4$/C nanocomposite films annealed at different temperatures (500 °C, 600 °C, and 700 °C) and the XRD patterns of the films at increasing annealing temperature. The as-synthesized $LiFePO_4$ were found to be amorphous and adopt an olivine phase with a crystallite size of ~20 nm when the temperature reached 600 °C. The crystallite size increased to ~30 nm at 800 °C. No peaks corresponding to carbon were seen in the XRD. This implies the carbon is amorphous and its presence does not bring any detectable influence on the crystal structure of $LiFePO_4$. A careful EDX analysis revealed the carbon in the films takes the form of particles homogenously distributed on the surface of $LiFePO_4$ crystallites.[16]

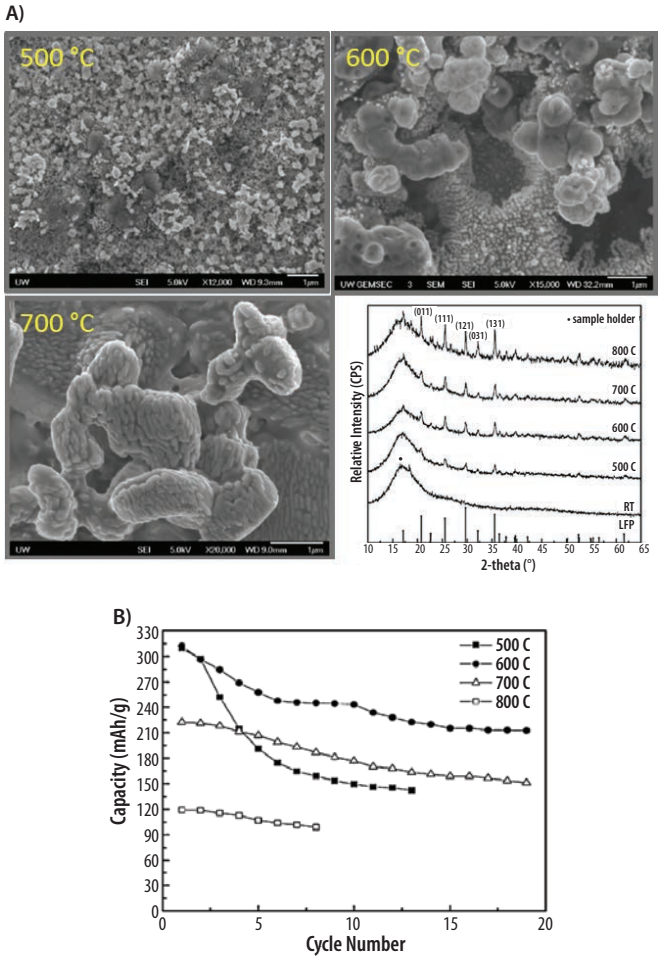

Figure 8. $LiFePO_4$/C nanocomposite for lithium ion battery. **A)** SEM images and XRD patterns and **B)** cyclic discharge capacities of $LiFePO_4$/C nanocomposite films annealed at different temperatures.[16]

Figure 8A shows a comparison of the cyclic discharge capacity of the $LiFePO_4$/C nanocomposite films annealed at different temperatures. Despite the high initial capacity, the sample annealed at 500 °C presented poor cyclic stability. The capacity dropped rapidly and reached 139 mAh/g after 13 cycles. This is attributed to the insufficient crystallinity of the film annealed at 500 °C. The best performance was achieved for samples annealed at 600 °C, which demonstrated the highest capacities of ~312 mAh/g for the initial cycle and approximately constant capacity of 218 mAh/g after 20 cycles. Annealing at higher temperatures, 700 °C and 800 °C, resulted in a significant decrease in capacity (228 mAh/g and 120 mAh/g for the initial cycle, dropping to 148 mAh/g and 99 mAh/g after 20 cycles). It is believed that 600 °C is the optimal temperature for annealing the $LiFePO_4$/C nanocomposite film because it gives rise to a slightly less crystallized/less compact structure that can accommodate more lithium ions and facilitate diffusion within the film.[16] Although films annealed at higher temperatures (e.g., 700 °C and 800 °C) possessed better crystallinity, their compact structure and decreased internal surface area delivered capacities lower than that of film annealed at 600 °C. This is also consistent with the trend observed with TiO_2 nanotube arrays produced with an anodization method discussed earlier.[6]

Conclusions and Remarks

Based on the above discussions, we can conclude that the capacity and cyclic stability of LIB technology rely heavily on the composition, morphology, crystal structure, and defects of the materials that form the electrode films. These parameters intrinsically affect the faradaic reaction occurring at solid–liquid interfaces and the electron/ion transport within batteries, and they are dependent on method of synthesis and post-treatment.

Internal Surface Area

Based on the results on MnO_2 nanowall arrays, TiO_2 nanotube arrays, V_2O_5 nanofibers, and V_2O_5 nanoporous films, it can be clearly seen that the morphology of materials, which primarily depends on the method of synthesis, plays a key role in determining the internal surface area. High surface area is usually the primary determinant of a material's performance in LIBs, as it allows for a large solid–liquid interface between the electrode films and electrolyte, enabling an efficient faradaic reaction. In addition to the synthesis method, which primarily determines the material's morphology, post-treatment such as annealing temperature and atmosphere also present an effective way to tailor the material's morphology. High internal surface area and the appropriate porosity benefit LIB performance by allowing the lithium ions to diffuse and to intercalate/deintercalate efficiently, contributing to high capacity.

Pathways for Electron and Ion Transport

The morphology of the materials used in batteries also influences the pathways of transport of electrons and lithium ions. In this aspect, 1D nanostructures present an obvious advantage over nanoparticles due to a significant reduction in the number of grain boundaries encountered during the electron or ion transport within electrode films. This makes the redox reaction in relation to lithium-ion intercalation and deintercalation more efficient, which allows batteries to be made with higher capacity. However, for electrode films with 1D nanomaterials, one usually needs to balance the trade-off between direct pathways for highly efficient transport and lower internal surface area provided by the 1D nanomaterials.

Crystallinity

Crystal structure or crystallinity is another issue closely related to the synthesis method and post-treatment. The use of amorphous materials for LIBs still seems to be up for debate. The MnO_2 nanowall arrays and TiO_2 nanotube arrays discussed above suggest amorphous materials may offer higher capacities compared to crystalline materials. This is because the relatively open structure of amorphous materials accommodates more lithium ions. However, as shown in the case of a TiO_2 nanotube, cyclic stability may be very poor for amorphous materials without heat treatment. It is generally observed that materials with better crystallinity possess better cyclic stability; whereas, higher capacity is achieved in less

well-crystallized materials. For example, for the $LiFePO_4$/C nanocomposites discussed above, the sample annealed at 600 °C demonstrated higher capacity than those annealed at 700 °C and 800 °C. In general, the crystallinity of a material is related to its electric conductivity. A less well crystallized material may contain some defects, such as oxygen vacancies, which lead to formation of an impurity energy level in the band gap and, therefore, lead to better conductivity than those perfectly crystallized materials. This enables higher capacity in a battery. It is worth pointing out that heat treatment at elevated temperatures not only reduces conductivity, it also causes the morphology to change. This usually corresponds to an increase in the size of crystallites and is a negative factor that diminishes the battery capacity due to a decrease in the internal surface area of the electrode film.

Defects

As mentioned above, the electric conductivity of the electrode film is related to its crystallinity via defect-induced impurity energy levels. The degree of defects formed in a material is affected by both the annealing temperature and the annealing atmosphere. It is shown that the use of CO and N_2 atmospheres during annealing of TiO_2 nanotubes and V_2O_5 xerogel films, respectively, introduces desired defects that result in the formation of low valence ions (e.g., Ti^{3+}, and V^{4+}, V^{3+}) and enhance the conductivity of electrode that leads to improvement in the battery capacity. The example of Mn-doped V_2O_5 film shows that in addition to controlling the annealing atmosphere, the use of a dopant during the material synthesis is also a way to introduce low valence ions and improve the battery performance.

References

(1) Johnson, C.; Dees, D.; Mansuetto, M.; Thackeray, M.; Vissers, D.; Argyriou, D.; Loong, C.-K.; Christensen, L. *Journal of power sources* **1997**, *68*, 570–577.
(2) Liu, D. W.; Zhang, Q. F.; Xiao, P.; Garcia, B. B.; Guo, Q.; Champion, R.; Cao, G. Z. *Chem. Mat.* **2008**, *20*, 1376–1380.
(3) Liu, D. W.; Garcia, B. B.; Zhang, Q. F.; Guo, Q.; Zhang, Y. H.; Sepehri, S.; Cao, G. Z. *Adv. Funct. Mater.* **2009**, *19*, 1015–1023.
(4) Mor, G. K.; Varghese, O. K.; Paulose, M.; Shankar, K.; Grimes, C. A. *Solar Energy Materials and Solar Cells* **2006**, *90*, 2011–2075.
(5) Roy, P.; Berger, S.; Schmuki, P. *Angewandte Chemie International Edition* **2011**, *50*, 2904–2939.
(6) Liu, D.; Xiao, P.; Zhang, Y.; Garcia, B. B.; Zhang, Q.; Guo, Q.; Champion, R.; Cao, G. *The Journal of Physical Chemistry C* **2008**, *112*, 11175–11180.
(7) Liu, D.; Zhang, Y.; Xiao, P.; Garcia, B. B.; Zhang, Q.; Zhou, X.; Jeong, Y.-H.; Cao, G. *Electrochimica Acta* **2009**, *54*, 6816–6820.
(8) Kim, D.; Ryu, H.; Moon, J.; Kim, J. *Journal of power sources* **2006**, *163*, 196–200.
(9) Fontenot, C. J.; Wiench, J. W.; Pruski, M.; Schrader, G. *The Journal of Physical Chemistry B* **2000**, *104*, 11622–11631.
(10) Liu, D.; Liu, Y.; Garcia, B. B.; Zhang, Q.; Pan, A.; Jeong, Y.-H.; Cao, G. *Journal of Materials Chemistry* **2009**, *19*, 8789–8795.
(11) Yu, D.; Zhang, S.; Liu, D.; Zhou, X.; Xie, S.; Zhang, Q.; Liu, Y.; Cao, G. *Journal of Materials Chemistry* **2010**, *20*, 10841–10846.
(12) Yu, D.; Chen, C.; Xie, S.; Liu, Y.; Park, K.; Zhou, X.; Zhang, Q.; Li, J.; Cao, G. *Energy & Environmental Science* **2011**, *4*, 858–861.
(13) Takahashi, K.; Wang, Y.; Cao, G. *The Journal of Physical Chemistry B* **2005**, *109*, 48–51.
(14) Wang, Y.; Cao, G. *Chem. Mat.* **2006**, *18*, 2787–2804.
(15) Liu, Y.; Clark, M.; Zhang, Q.; Yu, D.; Liu, D.; Liu, J.; Cao, G. *Advanced Energy Materials* **2011**, *1*, 194–202.
(16) Liu, Y.; Liu, D.; Zhang, Q.; Yu, D.; Liu, J.; Cao, G. *Electrochimica Acta* **2011**, *56*, 2559–2565.

Precursors for Lithium-ion Battery Materials Synthesis

Cobalt

For a complete list of available materials, visit aldrich.com/periodic.

Name	Composition	Purity	Form	Prod. No.
Cobalt(II) bromide, anhydrous	$CoBr_2$	99.99% trace metals basis	beads, −10 mesh	427136-1G 427136-5G
Cobalt(II) bromide	$CoBr_2$	99%	powder	334022-50G 334022-250G
Cobalt(II) carbonate hydrate	$CoCO_3 \cdot xH_2O$	99.99% trace metals basis	powder	379956-5G
Cobalt(II) chloride, anhydrous	$CoCl_2$	99.9% trace metals basis	beads, −10 mesh	449776-5G 449776-25G
Cobalt(II) chloride hydrate	$CoCl_2 \cdot xH_2O$, Degree of hydration 5-6	99.999% trace metals basis	powder and chunks	203084-10G
Cobalt(II) fluoride	CoF_2	-	powder	236128-25G
Cobalt(II) fluoride tetrahydrate	$CoF_2 \cdot 4H_2O$	99.99% trace metals basis	powder	399876-5G
Cobalt(II) hydroxide, technical grade	$Co(OH)_2$	95%	powder	342440-250G
Cobalt(II) iodide, anhydrous	CoI_2	99.999%	powder	499129-1G
Cobalt(II) nitrate hexahydrate	$Co(NO_3)_2 \cdot 6H_2O$	99.999% trace metals basis	crystals and lumps	203106-10G 203106-50G
Cobalt(II) oxalate dihydrate	$CoC_2O_4 \cdot 2H_2O$	-	powder	401285-10G 401285-50G
Cobalt(II) perchlorate hexahydrate	$Co(ClO_4)_2 \cdot 6H_2O$	-	crystals and lumps	401404-25G
Cobalt(II) sulfate hydrate	$CoSO_4 \cdot xH_2O$	99.998% trace metals basis	crystals and lumps	229598-10G

Iron

For a complete list of available materials, visit aldrich.com/periodic.

Name	Composition	Purity	Form	Prod. No.
Iron(II) bromide, anhydrous	$FeBr_2$	99.999% trace metals basis	beads, −10 mesh	434000-1G
Iron(III) bromide	$FeBr_3$	98%	powder	217883-10G 217883-50G
Iron(II) chloride, anhydrous	$FeCl_2$	99.998% trace metals basis	beads, −10 mesh	429368-1G 429368-10G
	$FeCl_2$	99.9% trace metals basis	beads, −10 mesh	450944-10G 450944-50G
Iron(II) chloride tetrahydrate	$FeCl_2 \cdot 4H_2O$	99.99% trace metals basis	crystals and lumps	380024-5G 380024-25G
Iron(III) chloride, anhydrous	$FeCl_3$	≥99.99% trace metals basis	powder	451649-1G 451649-5G
Iron(III) chloride, sublimed grade	$FeCl_3$	≥99.9% trace metals basis	powder or crystals	701122-1G 701122-5G 701122-25G
Iron(II) fluoride	FeF_2	98%	powder	399841-10G
Iron(III) fluoride	FeF_3	98%	powder	288659-10G
Iron(III) fluoride trihydrate	$FeF_3 \cdot 3H_2O$	-	powder	334499-25G
Iron(II) iodide, anhydrous	FeI_2	≥99.99% trace metals basis	beads, −10 mesh	400858-1G 400858-10G
Iron(III) nitrate nonahydrate	$Fe(NO_3)_3 \cdot 9H_2O$	≥99.999% trace metals basis	solid	529303-25G
Iron(II) oxalate dihydrate	$FeC_2O_4 \cdot 2H_2O$	99%	powder	307726-25G 307726-500G
Iron(III) oxalate hexahydrate	$Fe_2(C_2O_4)_3 \cdot 6H_2O$	-	powder and chunks	381446-5G 381446-25G
Iron(III) phosphate tetrahydrate	$FePO_4 \cdot 4H_2O$, Fe 24%	-	powder	436038-100G

Lithium

For a complete list of available materials, visit aldrich.com/periodic.

Name	Composition	Purity	Form	Prod. No.
Lithium bromide	LiBr	≥99.995% trace metals basis	powder and chunks	229733-25G 229733-125G
Lithium carbonate	Li_2CO_3	99.997% trace metals basis	powder	203629-10G 203629-50G
Lithium chloride	LiCl	≥99.99% trace metals basis	powder	203637-10G 203637-50G 203637-100G
Lithium fluoride	LiF	-	powder, -300 mesh	237965-100G 237965-1KG
Lithium hydroxide monohydrate	$LiOH \cdot H_2O$	99.95% trace metals basis	crystalline	254274-10G 254274-50G 254274-250G
Lithium iodide	LiI	99.9% trace metals basis	crystalline powder	518018-10G 518018-50G
Lithium nitrate	$LiNO_3$	99.99% trace metals basis	crystalline powder	229741-25G 229741-125G
Lithium phosphate	Li_3PO_4	-	powder	338893-100G
Lithium sulfate	Li_2SO_4	≥99.99% trace metals basis	solid	203653-10G

Manganese

For a complete list of available materials, visit aldrich.com/periodic.

Name	Composition	Purity	Form	Prod. No.
Manganese(II) chloride, anhydrous	$MnCl_2$	99.99% trace metals basis	beads, –10 mesh	429449-5G 429449-25G
Manganese(II) chloride	$MnCl_2$	≥99% trace metals basis	powder and chunks	244589-10G 244589-50G 244589-250G
Manganese(II) fluoride, anhydrous	MnF_2	99.99% trace metals basis	powder	771619-5G
Manganese(III) fluoride	MnF_3	99.9% trace metals basis	powder	339296-10G
Manganese(II) iodide, anhydrous	MnI_2	99.9%	powder	551619-1G
Manganese(II) nitrate hydrate	$Mn(NO_3)_2{\cdot}xH_2O$, Degree of hydration 4-6	99.99% trace metals basis	crystals and lumps	203742-25G 203742-100G
Manganese(II) perchlorate hydrate	$Mn(ClO_4)_2{\cdot}xH_2O$	99%	crystalline	359386-100G
Manganese(II) sulfate hydrate	$MnSO_4{\cdot}xH_2O$	≥99.99% trace metals basis	solid	229784-25G 229784-100G

Nickel

For a complete list of available materials, visit aldrich.com/periodic.

Name	Composition	Purity	Form	Prod. No.
Nickel(II) acetate tetrahydrate	$Ni(OCOCH_3)_2 \cdot 4H_2O$	≥99.0%, KT	powder or crystals	72225-250G 72225-1KG
Nickel carbonate, basic hydrate	$NiCO_3 . 2Ni(OH)_2 \cdot xH_2O$	99.9% trace metals basis	powder	544183-250G-A 544183-1KG-A
Nickel(II) chloride, anhydrous	$NiCl_2$	99.99% trace metals basis	powder	451193-5G 451193-25G
Nickel(II) chloride	$NiCl_2$	98%	powder	339350-50G 339350-250G
Nickel(II) chloride hexahydrate	$NiCl_2 \cdot 6H_2O$	99.999% trace metals basis	crystals and lumps	203866-5G 203866-25G
Nickel(II) hydroxide	$Ni(OH)_2$	-	powder	283622-250G 283622-1KG
Nickel(II) nitrate hexahydrate	$Ni(NO_3)_2 \cdot 6H_2O$	99.999% trace metals basis	solid	203874-20G 203874-100G 203874-500G
Nickel(II) sulfamate tetrahydrate	$Ni(SO_3NH_2)_2 \cdot 4H_2O$	98%	solid	262277-500G
Nickel(II) sulfate, anhydrous	$NiSO_4$	99.99% trace metals basis	solid	656895-10G 656895-50G
Nickel(II) sulfate heptahydrate	$NiSO_4 \cdot 7H_2O$	99.999% trace metals basis	crystals and lumps	203890-10G 203890-50G